Chemical Science

ROYAL SOCIETY OF CHEMISTRY

EDGE ARTICLE

View Article Online
View Journal | View Issue

Cite this: *Chem. Sci.*, 2020, **11**, 7468

All publication charges for this article have been paid for by the Royal Society of Chemistry

Diagnosing surface *versus* bulk reactivity for molecular catalysis within metal–organic frameworks using a quantitative kinetic model†

Ben A. Johnson * and Sascha Ott *

Received 7th May 2020
Accepted 25th June 2020

DOI: 10.1039/d0sc02601h

rsc.li/chemical-science

Metal–organic frameworks (MOFs) are becoming increasingly popular as heterogenous support matrices for molecular catalysts. Given that reactants, or potentially holes/electrons, need to diffuse into the porous framework as the reaction proceeds, the reaction can possibly take place within the bulk of the particle or be confined to a thin layer at the surface due to transport limitations. Herein, a simple steady-state reaction-diffusion kinetic model is developed to diagnose these two mutually exclusive behaviors in MOF-based systems. The oxygen evolution reaction (OER) driven by a chemical oxidant is presented as an example mechanism. Quantitative metrics for assigning either bulk or surface reactivity are delineated over a wide variety of conditions, and numerical simulations are employed to verify these results. For each case, expressions for the turnover frequency (TOF) are outlined, and it is shown that surface reactivity can influence measured TOFs. Importantly, this report shows how to transition from surface to bulk reactivity and thus identifies which experimental parameters to target for optimizing the efficiency of MOF-based molecular catalyst systems.

Introduction

Metal–organic frameworks (MOFs) are rapidly being explored as potential catalysts for a variety of important chemical transformations. Their high internal surface area could indeed result in extraordinarily high concentration of active sites. Furthermore, incorporation of highly active and selective molecular catalysts into MOF structures, *via* a variety of post-synthetic methods,[1,2] is possible due to the modularity of the organic linkers. This is advantageous as it can stabilize the molecular catalyst and avoid undesired bimolecular decomposition reactions, while providing a heterogeneous support matrix with a high density of anchoring sites. MOF-supported molecular catalysis has been previously demonstrated for energy related processes[3–6] including proton reduction,[7–9] CO_2 reduction,[10–14] and water oxidation,[15–20] as well as a variety of organic transformations with high-value products.[21–25]

However, given the interfacial nature of the reactions occurring in MOFs, mass and charge transport by a diffusional process are required to shuttle reactants, substrates, as well as electrons or holes to the molecular active sites in the MOF interior. As a result, situations arise where the catalytic reaction may be confined to the first few molecular layers or possibly even the surface of the particle. Determining where the reaction is occurring and what fraction of the imbedded molecular catalysts are active during the reaction is a prerequisite in order to take advantage of the high internal surface area displayed by MOF materials. Clearly, transport-limited or surface confined reactions would severely underutilize the large number of active sites within the MOF interior. Overcoming these limitations is of utmost importance not only to the efficiency but also to the performance (observed rate) and applicability of these materials to large-scale catalytic processes.[26] Transport phenomena are often overlooked in kinetic studies of MOF-based catalysis. Indeed, only a handful of remarkable reports[16,27–29] have accounted for these effects.[30] Moreover, kinetic models integrating diffusional processes along with mechanistic details for the immobilized molecular catalysts are lacking. As a result, whether the reaction occurs exclusively near the surface of the particle due to transport limitations or throughout the bulk of the particle remains an open question for many MOF-catalysed reactions.

Choosing the oxygen evolution reaction (OER) driven by a (photo)chemical oxidant as an example, herein we develop a quantitative reaction-diffusion kinetic model to diagnose either surface or bulk reactivity occurring with a molecular catalyst homogenously dispersed inside MOF particles. To the best of our knowledge, the present study is the first of its kind that summarizes the vast array of possible kinetic behaviours, and discusses means to distinguish between these different scenarios.

Department of Chemistry, Ångström Laboratory, Uppsala University, Box 523, 751 20 Uppsala, Sweden. E-mail: ben.johnson@kemi.uu.se; sascha.ott@kemi.uu.se

† Electronic supplementary information (ESI) available: Glossary of terms, simulated results, and complete derivations of reaction-diffusion kinetic models. See DOI: 10.1039/d0sc02601h

MOF-catalyst materials have been utilized extensively as micro-crystalline powders (particle sizes ranging from approximately 0.1 to 2 μm) suspended in solution. For energy related applications, a sacrificial chemical reagent (usually a strong oxidant or reductant) drives the reaction,[16,18,19] or in a photochemical assay,[9–11,14] a reducing or oxidizing photosensitizer is generated by quenching from a sacrificial donor or acceptor, respectively. In either case the oxidant or reductant must either physically diffuse through the pores or initiate a charge hopping process[31,32] that delivers electrons or holes to the catalytic sites in the interior of the particles to generate the active form of the catalyst. It is well-known that such a charge hopping process is formally diffusional, obeying Fick's laws.[33,34] Therefore, regardless of the pore structure of the MOF, substrates, chemical reagents, and/or electrons or holes will need to diffuse through the particles as the catalytic reaction proceeds (relevant scenarios are shown in Fig. 1). The resulting balance between reaction and diffusion will determine the overall rate and the surface *vs.* bulk reactivity of the MOF-catalyst construct (*i.e.*, the location and size of the boundary layer in the particle where the reaction occurs). With diffusion present, the interplay of a large number of variables determines the overall kinetic behaviour, often leading to non-intuitive results. Consequently, by qualitative reasoning alone, it may not be apparent how a single variable, such as the concentration of a specific reactant or the size of the particle, affects the observed catalytic activity and efficiency.

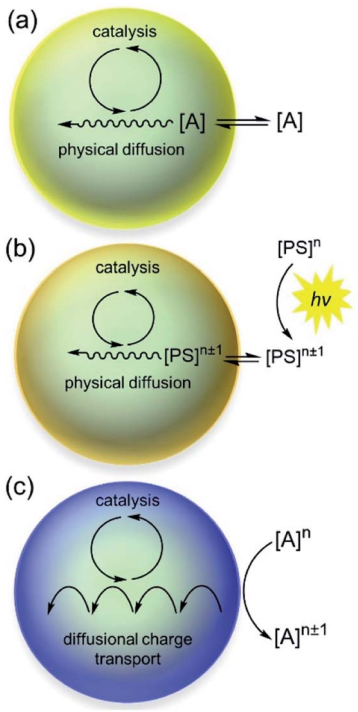

Fig. 1 Schematic representation of steady reaction-diffusion occurring within MOF particles with an imbedded molecular catalyst. (a) Chemically driven by a sacrificial oxidizing or reducing agent [A]. (b) Photochemically driven *via* a quenching process with a photosensitizer $[PS]^n$ that generates a highly oxidizing or reducing species $[PS]^{n\pm1}$. (c) Same as in part a or b; however, now the oxidant/reductant or photosensitizer is too large to enter the MOF pores, and reducing or oxidizing equivalents are transported to the catalytic sites *via* a charge hopping mechanism, described by an apparent diffusion coefficient, D_e.

In the present example, we define a small number of dimensionless parameters, which make it possible to identify which variables control the balance between chemical reactions and diffusion in each case and thus control the overall performance of the catalyst particle. We then elucidate quantitative relationships between the observed catalytic rate and the particle size, catalyst loading, and oxidant concentration. Numerical simulations are employed to confirm these relationships. Furthermore, we use these diagnostic criteria to illustrate how to assign the kinetic regime as: (1) surface reactivity, or (2) bulk reactivity. This allows one not only to extract relevant kinetic data (rate constants and diffusion coefficients) but to also identify which experimental variables to change in order to optimize the system for the highest efficiency and performance. We apply these tools and concepts to the present problem of supported molecular OER catalysis taking place within MOF particles, building on precedent from heterogenous catalysis and chemical reaction engineering. For example, efficiency, commonly quantified by the "effectiveness factor,"[35,36] is a measure of catalyst utilization, *i.e.*, what percentage of the immobilized molecular catalysts within the MOF particle participate in the reaction (*vide infra*). When diffusional transport limitations give rise to surface reactivity, the efficiency of the MOF-catalyst will become less than unity. Particular attention will be paid to the contribution of catalyst oxidation/activation by the external oxidant to the overall rate law. As will be shown, the concentration of oxidant or holes (*via* charge hopping) may be depleted within the particle significantly, which will decelerate these reactions to the point where they become rate-determining. Furthermore, we demonstrate that different values for the turnover frequency (TOF) can be obtained in the limit of either surface reactivity or bulk reactivity. The scenario where the oxidant can penetrate and diffuse into the MOF pores is examined first, followed by the case where the pore aperture size of the MOF is small and the oxidant is excluded from entering the particle. In case of the latter, a heterogeneous reaction at the particle–solution interface initiates the diffusional charge hopping process that supplies holes to the molecular catalyst.

The oxygen evolution reaction is used as an example; however, the fundamental principles of reaction-diffusion arising in catalytic MOF particles outlined here for diagnosing surface or bulk activity can be easily extended to other mechanisms involving fuel forming reactions (hydrogen evolution, CO_2 reduction) or a variety of catalytic organic transformations where there exists a sacrificial or limiting reactant.

Results and discussion

(Photo)chemically driven OER

Two mechanistic pathways (Fig. 2) are most often proposed for molecular water oxidation catalysis: water nucleophilic attack (WNA) and radical coupling (I2M). Additionally, the most active

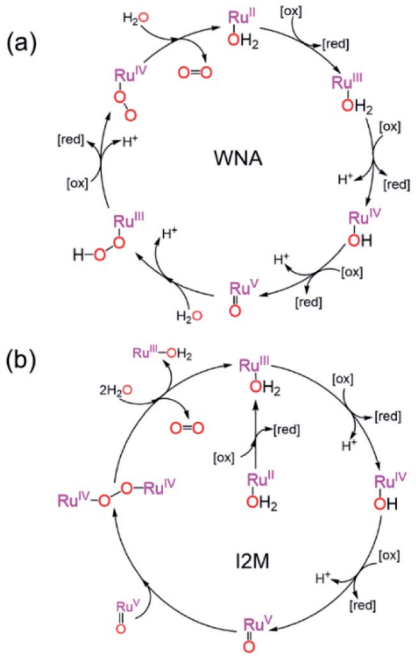

Fig. 2 (a) Water nucleophilic attack (WNA) and (b) radical coupling (I2M) mechanisms for water oxidation by a ruthenium polypyridyl catalyst driven with a (photo)chemical oxidant at pH = 1. The oxidized and reduced form of the oxidant are denoted by [ox] and [red] respectively.

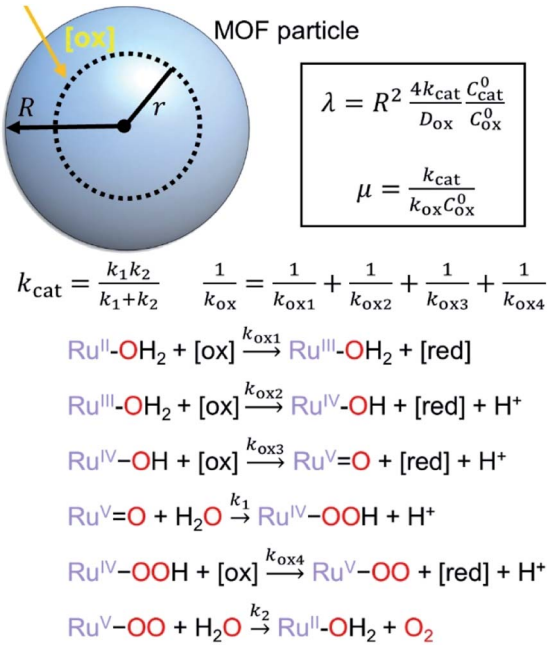

Fig. 3 Schematic diagram of MOF particle (top) with diffusing oxidant [ox] and generalized reaction scheme for WNA mechanism (bottom). As water is the solvent in addition to the substrate, its concentration is taken as large and constant both inside and outside the particle. Definitions of dimensionless governing parameters are given (top box).

molecular catalysts to-date are ruthenium-based transition metal complexes, typically featuring polypyridyl ligands.[37–39] Therefore, the two respective mechanisms displayed in Fig. 2, determined previously for homogeneous Ru-based catalysts,[38,40,41] will serve as the basis for the analysis to follow considering reaction-diffusion when the molecular Ru-catalyst is incorporated into a MOF particle. These mechanisms are also relevant, since there have been several previous reports of molecular ruthenium catalyst incorporated into, for example, the MIL-101(Cr)[19] or UiO-67 frameworks,[18] which undergo OER in the presence of a chemical oxidant. There are also several notable examples of Ir-based catalysts in UiO frameworks.[15,16] For brevity, only the WNA mechanism is described in detail; although, as shown in the ESI,† the I2M mechanism exhibits the same general reaction-diffusion behaviour. The latter is however less relevant in the context of MOFs where the catalysts are often integral parts of the material and will thus not engage in bimolecular encounters.

Oxidant diffusion through the MOF pores

First we consider the situation where the aperture size of the MOF pores is sufficiently large to allow the oxidant (either a chemical oxidant or oxidized photosensitizer) to enter and diffuse through the MOF particles. The generalized reaction scheme for WNA is shown in Fig. 3. The concentration of oxidant in the solution (C^0_{ox}) is assumed to be constant over short times, *i.e.*, when measuring initial rates. Wang *et al.* reported a reaction-diffusion model to account for consumption of the oxidant in the bathing solution over longer timescales (10–60 min.) in an experimental system with first order kinetics with respect to the oxidant.[16] For the mechanisms displayed in Fig. 2, we will see in the present treatment how the order of reaction with respect to the oxidant can switch from between first order and zero order depending on both C^0_{ox} and the oxidant's concentration gradient within the particle. The total concentration of catalyst in the particle is C^0_{cat} (referred to as the "catalyst loading"), D_{ox} is the diffusion coefficient of the oxidant inside the MOF particle, R is the particle radius (approximated as spherical), N is the total number of individual MOF particles (see ESI† for calculation of N), k_{ox} is the second order rate constant of the slowest oxidation reaction between the catalyst and oxidant (see ESI† for derivation), k_1 is the pseudo-first order rate constant of the water nucleophilic attack step, and k_2 is the first order rate constant for the oxygen release step. Fast coordination of a water molecule follows the first order decay of the Ru^V-OO intermediate, which closes the catalytic cycle (Fig. 3). The observed rate constant for the catalytic reaction steps (excluding the oxidation reactions to form the active catalyst) can be written as $k_{cat} = (k_1 k_2)/(k_1 + k_2)$ in the case of WNA, where each step is first order with respect to the catalyst. Applying steady-state, as shown in the ESI,† the concentration of oxidant $C_{ox}(r)$ within the particle is a function of the radial distance r (with $r = 0$ taken as the centre of the particle and $r = R$ defined as the particle surface).

Two dimensionless parameters (μ and λ, Fig. 3) control the resulting concentration profile of oxidant inside the particle as well as the observed rate of the reaction, v in mol s^{-1} (measured as the production of O_2). The competition between the rate of the catalytic

reaction (k_{cat}) and the rate of oxidation to form the catalytically active species is represented by $\mu = k_{cat}/(k_{ox}C^0_{ox})$. Importantly, $\lambda = (4R^2k_{cat}C^0_{cat})/(D_{ox}C^0_{ox})$ captures the influence of diffusion on the catalytic reaction and is defined as the ratio of the catalytic reaction rate to the diffusion rate of the oxidant inside the MOF particle.

Interestingly, the system of coupled reactions (Fig. 3) results in kinetic behaviour that bears a strong resemblance to Michaelis–Menten kinetics[42–44] (as shown in the ESI,† this is also the case for the I2M mechanism under certain conditions). At low concentrations, $C_{ox}(r) \rightarrow 0$, the reaction kinetics are first-order in oxidant. This shifts to zero-order with respect to $C_{ox}(r)$ at higher "saturating" concentrations, at which point the reaction rate approaches a maximum value. Analogous to the Michaelis–Menten constant, the magnitude of μ determines at what concentration of oxidant the system is "saturated." This is shown in Fig. 4a, which plots the dimensionless kinetic rate expression $\widetilde{K_\theta}$ (see ESI† for derivation) as a function of the dimensionless oxidant concentration $\theta(r) = C_{ox}(r)/C^0_{ox}$ inside the particle. This is analogous to the traditional solution-phase kinetic rate law for the coupled chemical reaction occurring in parallel with diffusion of the oxidant through the MOF pores. The saturating concentration of oxidant is indicated by the vertical dashed line where $\mu = \theta(r)$ and the kinetics shift from first to zero-order. As $\theta(r) \rightarrow 1$, the rate approaches a maximum value (Fig. 4a, horizontal dashed line), which is approximately equal to the magnitude of λ (representing the intrinsic rate of the OER reaction attenuated by any interference from diffusion). If the solution oxidant concentration C^0_{ox} is increased significantly, for nearly all values of $\theta(r)$ the reaction kinetics become saturated or zero-order in oxidant (Fig. 4b, green line).

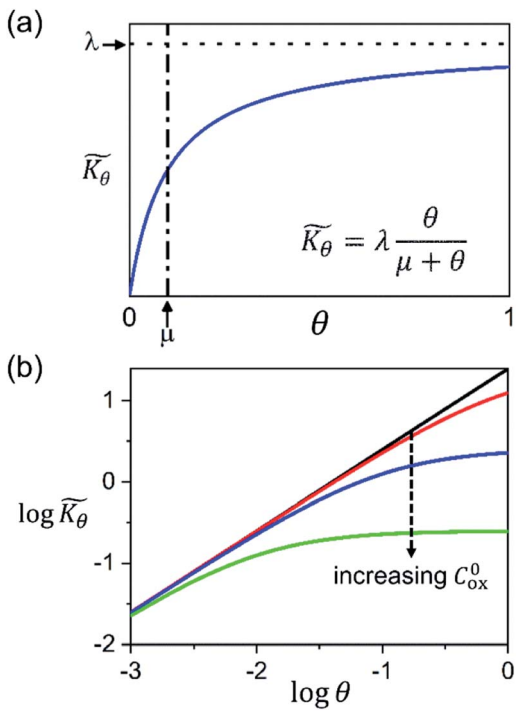

Fig. 4 (a) Plot of dimensionless kinetic term ($\widetilde{K_\theta}$), which represents the overall kinetics of the chemical reaction steps involving [ox], as a function of the dimensionless concentration ($\theta = C_{ox}(r)/C^0_{ox}$, *i.e.*, [ox] normalized to its concentration in the bathing solution). The vertical line shows the value of μ, which signals the change in reaction order in θ from first order to zero order. The horizontal line shows the maximum reaction rate set by λ. (b) Double logarithmic plot of $\widetilde{K_\theta}$ *vs.* θ for increasing values of C^0_{ox} (black: $\lambda = 250$, $\mu = 10$; red: $\lambda = 25$, $\mu = 1$; blue: $\lambda = 2.5$, $\mu = 0.1$; green: $\lambda = 0.25$, $\mu = 0.01$; in all cases: $\sqrt{\lambda/\mu} = 5$).

Approximate analytical solutions for the observed reaction rate (v), accounting for mass transport and the intrinsic kinetics of the oxidant/catalyst inside the MOF particle, can be obtained in various limiting situations by taking maximum or minimum values of the two dimensionless control parameters, λ and μ. For reference, each specific behaviour is assigned a zone (I to IV) with a corresponding closed-form expression for the observed rate. Numerical simulations are used to confirm the validity of the rate expressions.

Oxidant limited kinetics. We consider first the situation encountered when $\mu \gg 1$. This entails that C^0_{ox} is low enough so the rate of oxidation of the catalyst is unconditionally slower than the catalytic reaction ($k_{ox}C^0_{ox} < k_{cat}$). The overall kinetics of the system now depends only on a single dimensionless parameter $\sqrt{\lambda/\mu}$, which takes the form of the classical Thiele modulus[45] (eqn (1)).

$$\sqrt{\frac{\lambda}{\mu}} = R\sqrt{\frac{4k_{ox}C^0_{cat}}{D_{ox}}} \quad (1)$$

Regardless of the local concentration of oxidant, the kinetics are "unsaturated" throughout the particle (for all values of r) and first order with respect to $C_{ox}(r)$ (see Fig. 4b, black line).

Two limits can be found depending on the magnitude of $\sqrt{\lambda/\mu}$. When the activation of the catalyst by the oxidant, which is now the globally rate-determining chemical step, is slow compared to its diffusion rate through the MOF particle (reaction-controlled: $\sqrt{\lambda/\mu} \ll 1$), bulk reactivity is observed, and the oxidant is present at a nearly constant concentration throughout the particle approximately equal to its value in the bathing solution. The observed rate is trivially (zone I)

$$v = \frac{4}{3}N\pi R^3 k_{ox}C^0_{ox}C^0_{cat} \quad (2)$$

where N is the total number of MOF particles. On the other hand, if oxidation of the catalyst is much faster than the diffusion time of the oxidant (transport-controlled: $\sqrt{\lambda/\mu} \gg 1$), the overall rate becomes

$$v = N\pi R^2 C^0_{ox}\sqrt{D_{ox}}\sqrt{4k_{ox}C^0_{cat}} \quad (3)$$

In this regime (zone II), $C_{ox}(r)$ is depleted near the particle surface, due to its fast consumption before the oxidant is able to diffuse into the centre of the particle. A boundary or reaction-diffusion layer is formed near the surface, with a thickness given by $\delta_{rxn} = \sqrt{D_{ox}/4k_{ox}C^0_{cat}}$. Only catalytic sites contained within this thin layer are active, demonstrating surface reactivity as δ_{rxn} approaches the size of a monolayer. Using this definition of the boundary layer thickness, another way to characterize bulk reactivity is when the reaction-diffusion layer

is equal to or larger than the particle size ($\sqrt{D_{ox}/4k_{ox}C^0_{cat}} \geq R$). And in fact, $\sqrt{\lambda/\mu}$ is simply the ratio of these two length scales, *i.e.*, $\sqrt{\lambda/\mu} = R/\delta_{rxn}$.

These two behaviors can be easily differentiated experimentally by plotting the observed reaction rate (ν) as a function of the catalyst loading (C^0_{cat}) or the particle size (R). For bulk reactivity (zone I), a plot of ν *vs.* C^0_{cat} gives a linear relationship and indicates that the reaction is occurring throughout the particle. Whereas ν *vs.* $\sqrt{C^0_{cat}}$ will be linear if the kinetics are controlled by transport and the reaction is contained near the particle surface (zone II).[46,47] Similarly as expected, in the bulk reactivity regime the rate is proportional to R^3, indicating a dependence on the MOF particle's volume. When transport limitations are present, the observed rate will display proportionality to R^2, or the surface area of the particle.

In either case, the rate-determining chemical step is first order in $C_{ox}(r)$ ($\mu \gg 1$), making ν linearly proportional to C^0_{ox} under both bulk reactivity (reaction-controlled) and surface reactivity (transport-controlled) conditions. These diagnostic relationships are summarized in Table 1 using the order of the reaction rate with respect to each experimental variable. Transitions between each kinetic regime are summarized in the zone diagram in Fig. 7.

The efficiency η, canonically referred to as the internal effectiveness factor,[35,36,48] is defined as the ratio of the observed reaction rate to the maximum reaction rate (eqn (2)) in the absence of any diffusional gradients (see ESI eqn (S15) for further details†). This is a direct metric of how much of the catalyst is utilized or active in the reaction, as transport limitations fundamentally create boundary layers near the particle surface, outside of which the active catalyst concentration is essentially zero. Thus the primary effect of comparatively slow diffusion (when $\sqrt{\lambda/\mu}$ is large) is that it reduces the total amount of catalyst participating in the reaction at steady-state – *i.e.*, slow diffusion induces surface reactivity ($\eta \ll 1$ for surface reactivity, Fig. 5 zone II; $\eta = 1$ for bulk reactivity, Fig. 5 zone I). This is indeed a function of the particle size, since the oxidant will have a longer characteristic diffusion time ($t_{diff} \sim R^2/D_{ox}$) in particles with larger radii. The catalytic efficiency (or effectiveness factor) of the MOF particle as it varies with R is shown in Fig. 5.

Catalyst limited kinetics. In the opposite limit, when $\mu \ll 1$ or under saturated kinetics, the catalytic reaction step(s) become globally rate-determining ($k_{ox}C^0_{ox} \gg k_{cat}$). Either surface or bulk reactivity will dominate depending on the magnitude of λ. First, as $\lambda \ll 1$, the catalytic reaction is much slower than diffusion, and there is minimal depletion of oxidant within the particle. The reaction rate straightforwardly is given by eqn (4) (zone III; Fig. 6).

$$\nu = \frac{4}{3} N\pi R^3 k_{cat} C^0_{cat} \quad (4)$$

Now ν is independent of C^0_{ox} and is proportional to C^0_{cat} and the particle volume ($\nu \propto R^3$). Bulk reactivity is reached ($\eta = 1$), and the observed rate is controlled by the intrinsic rate of the catalytic reaction (k_{cat}). For that reason, kinetic data obtained under these conditions will be the most useful for benchmarking.

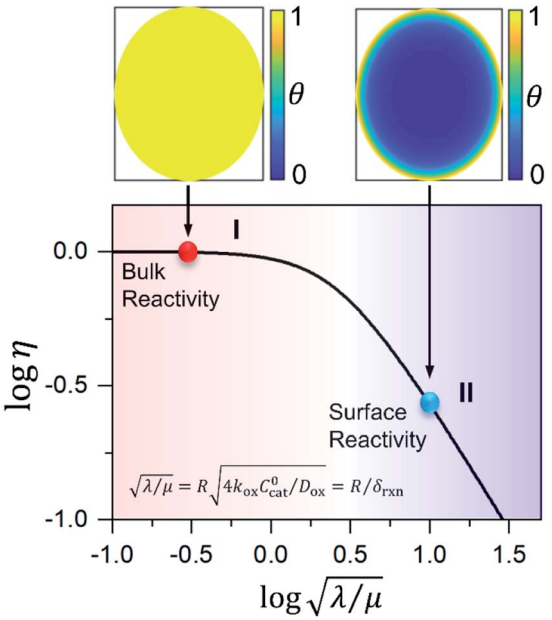

Fig. 5 Internal effectiveness factor η plotted as a function of the dimensionless control parameter $\sqrt{\lambda/\mu}$ relating the oxidant reaction kinetics to its rate of diffusion through the particle (oxidant limited kinetics, $\mu \gg 1$). Bulk reactivity (zone I) with 100% active catalyst is observed when $\eta = 1$. Surface reactivity (zone II) is shown when $\eta < 1$, indicating low catalyst utilization within the particle. Contour plots of the dimensionless concentration of oxidant inside the particle ($\theta(r) = C_{ox}(r)/C^0_{ox}$) for each respective case are shown above (colour key: yellow, $\theta = 1$; blue, $\theta = 0$).

Table 1 Diffusing oxidant: rate expressions and diagnostic criteria for limiting zones

Zone	Dimensionless rate $\tilde{\nu} = \nu/(N\pi RD_{ox}C^0_{ox})$	Rate ν (mol s^{-1})	Orders $\frac{\partial \log \nu}{\partial \log R}$	$\frac{\partial \log \nu}{\partial \log C^0_{ox}}$	$\frac{\partial \log \nu}{\partial \log C^0_{cat}}$
I	$\lambda/(3\mu)$	$\frac{4}{3}N\pi R^3 k_{ox} C^0_{ox} C^0_{cat}$	3	1	1
II	$\sqrt{\lambda/\mu}$	$N\pi R^2 C^0_{ox}\sqrt{D_{ox}}\sqrt{4k_{ox}C^0_{cat}}$	2	1	$\frac{1}{2}$
III	$\lambda/3$	$\frac{4}{3}N\pi R^3 k_{cat} C^0_{cat}$	3	0	1
IV	$\sqrt{2\lambda}$	$N\pi R^2\sqrt{D_{ox}}\sqrt{8k_{cat}C^0_{cat}C^0_{ox}}$	2	$\frac{1}{2}$	$\frac{1}{2}$

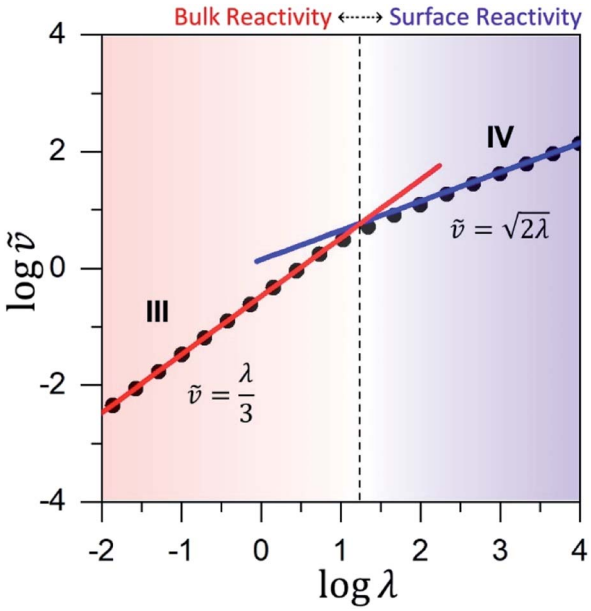

Fig. 6 Working curve for the observed reaction rate valid for catalyst limited kinetics when $\mu \leq 10^{-2}$. The vertical axis plots the dimensionless reaction rate $\tilde{v} = v/(N\pi RD_{ox}C^0_{ox})$, which varies as a function of $\lambda = (4R^2k_{cat}C^0_{cat})/(D_{ox}C^0_{ox})$. The vertical dashed-line shows the transition from surface reactivity (zone IV; shaded blue) to bulk reactivity (zone III; shaded red). The dimensionless rate expression for bulk reactivity with catalyst limited kinetics (solid red line; see eqn (4)) is plotted with the corresponding expression for surface reactivity (solid blue line; see eqn (5)). Results from the numerical simulations (black dots) are shown for comparison.

When diffusion becomes limiting, for large particles or slow diffusion $\lambda \gg 1$, again a boundary layer is present near the particle surface. The observed rate is shown in eqn (5) (zone IV; Fig. 6).

$$v = N\pi R^2\sqrt{D_{ox}}\sqrt{8k_{cat}C^0_{cat}C^0_{ox}} \quad (5)$$

Like the other cases of surface reactivity, the observed rate in eqn (5) is proportional to the surface area as well as to the square root of the diffusion coefficient. There is also a half-order dependence on both the catalyst loading[46,47] and the solution oxidant concentration, differentiating this situation from the unsaturated kinetic regime obtained with eqn (3) (zone II). A summary for these diagnostics can be found in Table 1 (also see the zone diagram in Fig. 7).

Similar to above, modifying the particle size (*i.e.*, varying λ) will allow one to transition from surface to bulk reactivity within the approximation of catalyst limited kinetics. This transition occurs around $\lambda \sim 20$ and is shown in Fig. 6 for small values of μ ($\leq 10^{-2}$). Surface reactivity (zone IV; Fig. 6) is observed when $\lambda > 20$, while for values of $\lambda < 20$, bulk reactivity persists (zone III; Fig. 6). Excellent agreement was found between the approximate analytical expressions for the observed rate in eqn (4) (Fig. 6, red line) or eqn (5) (Fig. 6, blue line) and the simulated results (Fig. 6, black dots).

Mixed kinetic control. A more complex situation arises if we consider $\mu \sim 1$. This is where the rates of the oxidation steps and the rate of the catalytic steps are approximately equal so that neither is predominantly limiting. First considering bulk reactivity, which is reached with fast diffusion and/or small particles ($\lambda \ll 1$), the dimensionless rate can be approximated by eqn (6).

$$\tilde{v} = \frac{\lambda}{3(\mu+1)} - \frac{\mu\lambda^2}{45(\mu+1)^3} \quad (6)$$

The validity of this solution can be checked and matches the limiting situations described in the previous sections. When μ is made either small or large, eqn (4) (zone III; catalyst limited kinetics) or eqn (2) (zone I; oxidant limited kinetics) are recovered respectively. This is confirmed by numerical simulations shown in Fig. S1.†

For large particles, when the reaction is confined at or near the surface of the particle ($\lambda \gg 1$), the dimensionless rate becomes

$$\tilde{v} = \sqrt{2\lambda\left(1 - \mu\ln\left(\frac{\mu+1}{\mu}\right)\right)} \quad (7)$$

Similar as above, this solution simplifies to the cases of oxidant limited kinetics described by zone II (eqn (3); $\mu \gg 1$) or catalyst limited kinetics described by zone IV (eqn (5); $\mu \ll 1$). The observed rate predicted by eqn (7) matches well with the numerical simulations (Fig. S2†). The transition between these behaviours for large particles ($\lambda = 10^4$) upon variation of μ is shown in Fig. 8. It should be noted that when the reaction kinetics become increasingly unsaturated ($k_{ox}C^0_{ox} \ll k_{cat}$) and the oxidation reaction is rate-determining and very slow (*i.e.*, $\sqrt{\lambda/\mu} < 1$), bulk reactivity is recovered (zone I; Fig. 8) and eqn (7) is no longer valid. Again, excellent agreement is found between the approximate analytical rate expressions for each limiting zone (Fig. 8, solid lines) and the numerical simulations (Fig. 8, black dots).

An interesting effect is caused by the depletion of the oxidant over the reaction-diffusion layer when $\lambda > 1$ and $\mu \sim 1$. Nearest to the particle surface the oxidant is present at higher concentrations and the kinetics are saturated $\theta(r) > \mu$. Progressing into the particle interior, as the oxidant is depleted over the reaction-diffusion layer, a change to unsaturated kinetics occurs when $\theta(r) < \mu$. In effect this means that near the surface, the rate-determining step will reflect the catalytic reaction (k_{cat}).

Conversely, within the interior of the particle the drop in oxidant concentration causes the oxidation of the catalyst to be rate-determining (k_{ox}). As a result, the nature of the rate-determining chemical reaction step will have a spatial dependence within the particle, simply because the concentration of one of the reactants changes significantly as a function of the distance from the surface.

Oxidant excluded from the MOF pores

Next, we turn our attention to diagnosing surface or bulk reactivity when the oxidant is size excluded from diffusing into the pores of the MOF. It would seem that this would trivially always result in surface reactivity; however, considering the redox-activity of many molecular catalysts, it is possible that oxidation of the sites at the particle–solution interface can

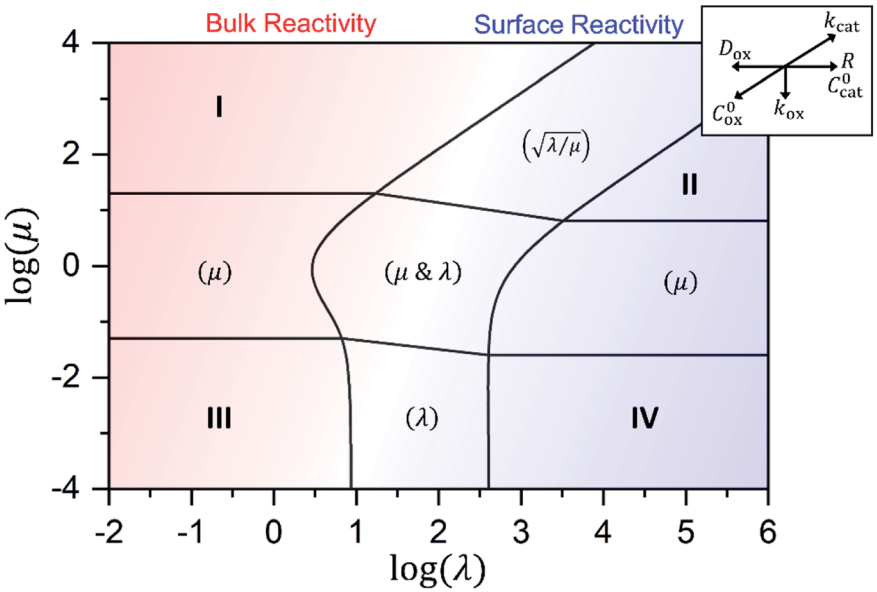

Fig. 7 Kinetic zone diagram for the case where oxidant is able to freely diffuse through the particle, with $\mu = k_{cat}/(k_{ox}C^0_{ox})$ and $\lambda = (4R^2k_{cat}C^0_{cat})/(D_{ox}C^0_{ox})$. Zones displaying bulk reactivity where nearly all the catalyst sites are active are shaded in red. Surface reactivity zones where a boundary layer ensues, which reduces the active catalyst, are shaded in blue. Each limiting zone, where the rate expression does not depend on either dimensionless parameter, is labelled with the corresponding numeral (I to IV; see Table 1 for rate equations). For intermediate cases, where the expression for $\tilde{\nu}$ depends on one or more dimensionless parameters, the controlling parameter(s) are shown in parentheses. Numerical simulations were used to compute the observed rate in zones were no analytical solution exists (central zone). The compass in the upper right displays the direction in which increasing a given experimental variable will translate the system within the zone diagram. The boundaries between zones are based on 5% error in the value of the observed steady-state reaction rate ($\tilde{\nu}$).

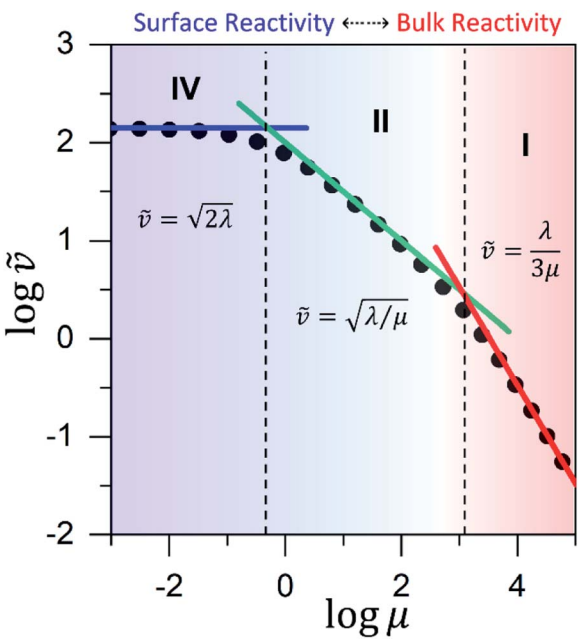

Fig. 8 Working curve for the observed reaction rate, valid for large particles and/or slow diffusion ($\lambda = 10^4$). The dimensionless reaction rate $\tilde{\nu} = \nu/(N\pi RD_{ox}C^0_{ox})$ is plotted against $\mu = k_{cat}/(k_{ox}C^0_{ox})$. The transitions between zones are indicated by the vertical dashed lines. Limiting rate expressions are represented by solid lines: (red line) bulk reactivity/unsaturated (zone I); (green line) surface reactivity/unsaturated (zone II); (blue line) surface reactivity/saturated (zone IV). Results from numerical simulations are shown for comparison (black dots).

initiate a diffusional charge hopping processes that carries holes into the interior. In this case, the molecular catalysts inside the particle are responsible for carrying out charge propagation in addition to the catalytic reaction.

To understand this situation in more detail we adopt a simplified mechanism (for WNA) displayed in Fig. 9. Here, the catalytic resting state, a nominal $Ru^V{=}O$ intermediate, is generated by diffusional charge hopping. This intermediate typically reacts with H_2O in a turnover limiting O–O bond formation step[40,49] (k_1 in s^{-1}, Fig. 9). The substrate (H_2O), as before, is assumed to maintain a constant concentration. Catalysis proceeds further by a sequence of follow-up reactions (either re-oxidation by charge hopping or purely chemical steps) that are considered to be fast and thus do not appear in the observed rate law. Accounting for the $4e^-$ stoichiometry of the OER, the observed rate constant is $k_{cat} = 4k_1$.

Taking into consideration the heterogeneous interfacial oxidation reaction and diffusional hole hopping inside the MOF particle requires defining two new dimensionless parameters. The first parameter reflects the classical Thiele modulus,

$$\lambda_e = R\sqrt{\frac{k_{cat}}{D_e}} \quad (8)$$

where D_e is the apparent diffusion coefficient for charge transport between molecular catalysts within the MOF. The second parameter, γ, represents the competition between the heterogeneous reaction involving the oxidant/catalyst and diffusional charge transport:

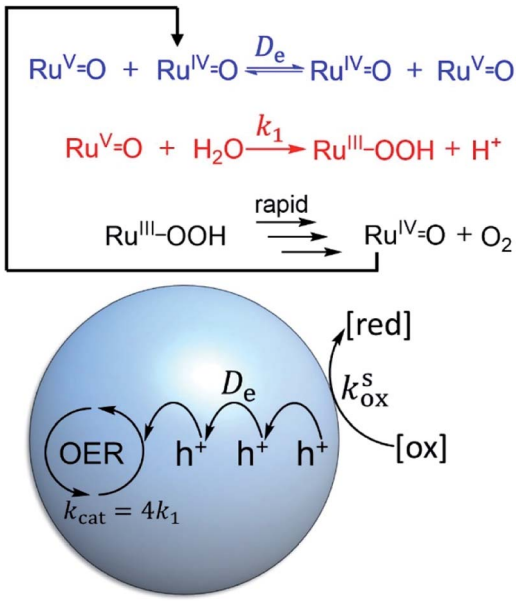

Fig. 9 Simplified WNA mechanism (top) where holes (h+) are supplied to the imbedded molecular catalysts by diffusional charge transport (self-exchange) with an apparent diffusion coefficient D_e. The pores of the MOF are small enough to prevent the external oxidant from entering and diffusing through the particle (bottom). A heterogeneous reaction with rate constant k^s_{ox} at the particle–solution interface initiates charge propagation.

$$\gamma = R\frac{k^s_{ox}C^0_{ox}}{D_e} \tag{9}$$

Now, k^s_{ox} is defined as a second order heterogeneous rate constant ($cm^4\ mol^{-1}\ s^{-1}$). Looking at these two control parameters, it is apparent that the reaction-diffusion behaviour of the system will not directly depend on the catalyst loading C^0_{cat}, when the oxidant is unable to enter the MOF pores. We note, however, that the catalyst loading may have an indirect effect, as the apparent diffusion coefficient for charge transport will likely have a dependence on the total concentration of redox-active sites.[50] However, the active catalyst concentration $C_{Ru(V)}$ is a function of distance r and may be depleted within the particle. Additionally, the solution concentration of oxidant C^0_{ox} only affects the heterogeneous reaction at the interface (it is not diffusing inside the framework).

As shown in the ESI,† by taking into account the appropriate boundary conditions, limiting behaviours can be found for large or small values of λ_e and γ. The transition between these reciprocal kinetic regimes (labelled V through VII) is represented in the zone diagram in Fig. 10. Rate expressions and diagnostic criteria are summarized in Table 2.

A new case is established when the heterogeneous reaction rate to activate the catalyst, *i.e.* the hole injection into the particle, is slow compared to the rate of diffusional charge transport (zone V). It follows that $\gamma \to 0$, and the observed rate is found to only depend on the interfacial reaction:

$$v = 4N\pi R^2 k^s_{ox}C^0_{ox}C^0_{cat} \tag{10}$$

Catalysis can either take place in the bulk of the particle (zone V(a); small λ_e and $C_{Ru(V)}(r) = C^0_{cat}$ for all r) or in a boundary layer at the surface (zone V(b); large λ_e); however, the observed rate is gated by the oxidation of the catalyst at the particle–solution interface. Diagnostics for this situation, both V(a) and V(b), are first order behaviour in both catalyst and oxidant (see Table 2), making this similar to the bulk reactivity case with unsaturated kinetics for a freely diffusing oxidant in the previous section (zone I; eqn (2)). The discriminating feature is that the rate in eqn (10) will depend on the surface area of the particle ($\propto R^2$) rather than the volume ($\propto R^3$), and this allows one to assign the heterogeneous oxidation reaction (k^s_{ox}) as rate-determining and that a diffusional charge hopping mechanism is operative.

As mentioned above, λ_e controls the variation between bulk and surface reactivity as diffusional charge transport becomes slower than the catalytic reaction and causes the oxidized form of the catalyst to be confined to a thin layer near the surface. The expression for the observed rate (as $\gamma \to \infty$) under bulk reactivity (zone VI), and surface reactivity (zone VII), are displayed in eqn (11) and eqn (12) respectively.

$$v = \frac{4}{3}N\pi R^3 k_{cat}C^0_{cat} \tag{11}$$

$$v = 4N\pi R^2 C^0_{cat}\sqrt{D_e k_{cat}} \tag{12}$$

When surface reactivity is observed, the reaction-diffusion layer thickness can be defined as $\delta_{rxn} = \sqrt{D_e/k_{cat}}$. In both these cases, since diffusional charge transport carries holes into the MOF particle, the rate is independent of the solution concentration of the oxidant. Furthermore, as expected for bulk reactivity in the absence of other limiting factors (oxidation kinetics, diffusion), eqn (11) is identical to that for zone III (eqn (4)) when the oxidant can diffuse through the framework. In these limits, the system only depends on the intrinsic catalytic reaction, which is the ideal operating condition for applications and catalyst benchmarking. Nevertheless, one way to confirm if the oxidant is penetrating and diffusing within the particle or if it is excluded and a charge hopping mechanism is present is to systematically increase the particle size and traverse into a regime where diffusion begins to affect the kinetics (entering either zone IV or zone VII).

Surface *vs.* bulk reactivity and measured TOFs

A typical metric used in the kinetic characterization of molecular catalysts incorporated into MOFs is the turnover frequency (TOF). The classical definition of TOF for homogeneous solution phase catalytic reactions is the moles of product generated per unit time divided by the total moles of catalyst present. We have shown here that the possibility of surface reactivity arises due to the coupling of the catalytic reaction to diffusion within the MOF particle, and the *active* catalytic species are then confined in a reaction layer near the particle surface. Therefore, TOFs obtained taking into account the total amount of catalyst may not reflect the actual activity of the incorporated molecular catalyst. In order to make this distinction more clear, two

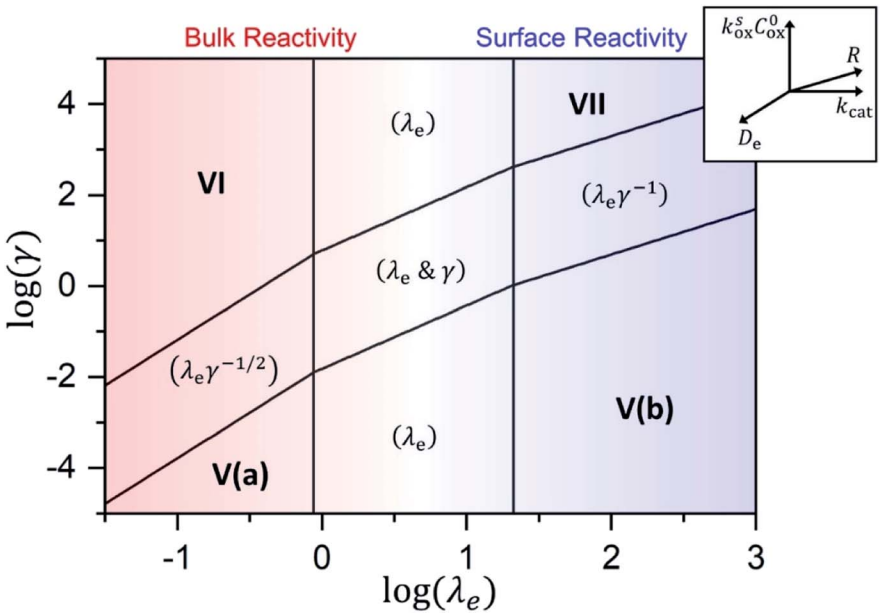

Fig. 10 Kinetic zone diagram for the case where oxidant is unable to enter particle due to size restrictions. The influence of the heterogeneous oxidation reaction by [ox] at the particle–solution interface is controlled by the dimensionless parameter $\gamma = R(k^s_{ox}C^0_{ox}/D_e)$ on the vertical axis. The horizontal axis plots the classical Thiele modulus for the competition between the catalytic reaction and diffusional charge transport $\lambda_e = R\sqrt{k_{cat}/D_e}$. Zones displaying bulk reactivity where nearly all the catalyst sites are active are shaded in red. Surface reactivity zones where a boundary layer ensues, which reduces the active catalyst, are shaded in blue. Each limiting zone, where the rate expression does not depend on either dimensionless parameter, is labelled with the corresponding numeral (V to VII; see Table 2 for rate equations). For intermediate cases, where the expression for $\tilde{\nu}$ depends on one or more dimensionless parameters, the controlling parameter(s) are shown in parentheses. The compass in the upper right displays the direction in which increasing a given experimental variable will translate the system within the zone diagram. The boundaries between zones are based on 5% error in the value of the observed steady-state reaction rate ($\tilde{\nu}$).

definitions of TOF need to be adopted,[4,19] the apparent turnover frequency (TOF^{app}) and the true turnover frequency (TOF^{true}):

$$TOF^{app} = \frac{\nu}{m_{total}} = \frac{\nu}{(4/3)N\pi R^3 C^0_{cat}} \quad (13)$$

$$TOF^{true} = \frac{\nu}{m_{active}} \sim \frac{\nu}{4N\pi R^2 \delta_{rxn} C^0_{cat}} \quad (14)$$

where $m_{total} = (4/3)N\pi R^3 C^0_{cat}$ is the total moles of catalyst and $m_{active} \sim 4N\pi R^2 \delta_{rxn} C^0_{cat}$ is the moles of catalyst that effectively participate in the reaction within the reaction layer of thickness δ_{rxn}, and ν is the observed reaction rate (production of O_2 in mol s^{-1}) as defined previously.

The resulting expressions for TOF^{app} and TOF^{true} are presented in Table 3 for each zone, either bulk or surface reactivity, within the case of a diffusing oxidant as well as that for diffusional charge hopping. Zone V is not displayed because the observed rate is limited by the heterogeneous oxidation reaction at the particle–solution interface rather than the reactions taking place within the interior of the particle. It is readily apparent that when the MOF-catalyst displays surface reactivity due to diffusional limitations on the reaction rate, TOF^{app} deviates from an intrinsic kinetic value and is a function of both the particle size (R) and a particular diffusivity (D_{ox} or D_e). For example, it was found in every case of surface reactivity, TOF^{app} will decrease with increasing particle size ($TOF^{app} \propto R^{-1}$; zones II, IV, and VII), as an increasing proportion the catalysts are outside δ_{rxn}. In some situations where the oxidant freely diffuses through the particle, TOF^{app} may also even depend on the catalyst concentration itself (see zones II and IV). These results show that TOF^{app} is not ideal for characterizing intrinsic kinetics; however, observing a dependence of TOF^{app} on the

Table 2 Size excluded oxidant (charge hopping): rate expressions and diagnostic criteria for limiting zones

Zone	Dimensionless rate $\tilde{\nu} = \nu/(N\pi RD_eC^0_{cat})$	Rate ν (mol s^{-1})	Orders $\frac{\partial \log \nu}{\partial \log R}$	$\frac{\partial \log \nu}{\partial \log C^0_{ox}}$	$\frac{\partial \log \nu}{\partial \log C^0_{cat}}$
V (a & b)	γ	$4N\pi R^2 k^s_{ox} C^0_{ox} C^0_{cat}$	2	1	1
VI	$\frac{\lambda_e{}^2}{3}$	$\frac{4}{3}N\pi R^3 k_{cat} C^0_{cat}$	3	0	1
VII	λ_e	$4N\pi R^2 C^0_{cat}\sqrt{D_e k_{cat}}$	2	0	1

Table 3 Expressions for TOF^{app} and TOF^{true} in each limiting kinetic zone[a,b]

Diffusing oxidant			
Zone	TOF^{app} (s^{-1})	TOF^{true} (s^{-1})	δ_{rxn}
I	$k_{ox}C^0_{ox}$	$k_{ox}C^0_{ox}$	$\geq R$
II	$\frac{3}{2R}C^0_{ox}\sqrt{\frac{2D_{ox}k_{ox}}{C^0_{cat}}}$	$k_{ox}C^0_{ox}$	$\sqrt{\frac{D_{ox}}{4k_{ox}C^0_{cat}}}$
III	k_{cat}	k_{cat}	$\geq R$
IV[b]	$\frac{3}{2R}\sqrt{\frac{2D_{ox}k_{cat}C^0_{ox}}{C^0_{cat}}}$	$\sim k_{cat}$	$\sim\sqrt{\frac{D_{ox}C^0_{ox}}{4k_{cat}C^0_{cat}}}$

Size excluded oxidant (charge hopping)			
Zone	TOF^{app} (s^{-1})	TOF^{true} (s^{-1})	δ_{rxn}
VI	k_{cat}	k_{cat}	$\geq R$
VII	$\frac{3}{R}\sqrt{D_e k_{cat}}$	k_{cat}	$\sqrt{\frac{D_e}{k_{cat}}}$

[a] Zones of bulk reactivity are shaded red, while surface reactivity zones are shaded blue. [b] Calculation of TOF^{true} in zone IV is presented as an estimate, since the reaction layer thickness (δ_{rxn}) is not well-defined due to the non-linear chemical reaction kinetics. The expressions given here are first order approximations as indicated in the table (see ESI for details).

particle size can be used as a diagnostic for surface reactivity. Conversely, by approximating the size of the reaction layer (δ_{rxn}), which depends on the reaction-diffusion behavior characteristic of each zone, TOF^{true} reflects an intrinsic kinetic parameter even under conditions of surface reactivity. Finally, when the experimental variables are optimized and bulk reactivity is obtained, TOF^{app} will be independent of the particle size and approximately equal to TOF^{true}. Under bulk reactivity, both these metrics reflect the kinetic properties of the molecular catalyst inside the MOF pore structure (Table 3; zones III, and VI).

These distinctions in TOF values are particularly important for benchmarking the activity of different MOF-based catalysts. The quantitative analysis presented here demonstrates that the most useful information can be obtained by comparing intrinsic kinetic parameters (TOF^{true}) in combination with metrics for catalyst efficiency in terms of bulk *versus* surface reactivity (*e.g.*, the effectiveness factor, η; Fig. 5). Furthermore, the microenvironment inside the MOF pore may have a significant influence on the activity of the incorporated molecular catalyst by augmenting its outer coordination sphere. Characterizing this effect may mean comparing the activity of the MOF-imbedded species to the homogeneous analogue, where the intrinsic rate of the catalyst (TOF^{true}) in each environment, decoupled from mass and charge transport, is of the most value.

Conclusions

At present, quantitative kinetic studies of MOF-based catalysis are scarce. The interaction of a number of chemical processes including transport phenomena convolute the analysis, and simple predictions as to how the observed rate will respond to changes in reactant concentration, particle size *etc.* may become non-intuitive. However, as shown here, kinetic evaluation is a necessary step towards the productive utilization of MOFs as support matrices for molecular catalysts. Despite having the possibility for a high density of active sites in MOFs, this advantage may be underutilized under certain conditions. This is primarily because the reaction-diffusion characteristics of the MOF-catalyst construct determine how many of the imbedded catalysts within the particle participate in the reaction. In this report, taking OER as a target reaction mechanism, we have demonstrated a simple kinetic model to assess and diagnose bulk *vs.* surface reactivity. It was shown how to transition between these behaviours based on a small number of dimensionless parameters. By modifying certain quantities, for example the particle size,[45] this allows one to take full advantage of the unique material and structural properties of MOFs for highly efficient molecular catalysis. Thus, the quantitative analysis presented here serves as an illustrative example for examining the reaction-diffusion challenge at the heart of MOF-based catalysis and opens the doors for future kinetic studies of catalytic MOFs with a fundamental understanding of the transport phenomena and chemical mechanisms at play.

Conflicts of interest

There are no conflicts to declare.

Acknowledgements

Financial support from the European Research Council *via* Project ERC-CoG2015-681895_MOFcat is gratefully acknowledged. B.A.J. acknowledges Dr Vincent C.-C. Wang, Mr Robin Tyburski, and Dr Lei Tian for, as always, very stimulating discussions on the matter at hand.

Notes and references

1 S. M. Cohen, *J. Am. Chem. Soc.*, 2017, **139**, 2855–2863.
2 M. Kim, J. F. Cahill, Y. Su, K. A. Prather and S. M. Cohen, *Chem. Sci.*, 2012, **3**, 126–130.
3 C. A. Downes and S. C. Marinescu, *ChemSusChem*, 2017, **10**, 4374–4392.
4 B. D. McCarthy, A. M. Beiler, B. A. Johnson, T. Liseev, A. T. Castner and S. Ott, *Coord. Chem. Rev.*, 2020, **406**, 213137.
5 M. B. Majewski, A. W. Peters, M. R. Wasielewski, J. T. Hupp and O. K. Farha, *ACS Energy Lett.*, 2018, **3**, 598–611.
6 T. Zhang and W. Lin, *Chem. Soc. Rev.*, 2014, **43**, 5982–5993.
7 S. Roy, Z. Huang, A. Bhunia, A. Castner, A. K. Gupta, X. Zou and S. Ott, *J. Am. Chem. Soc.*, 2019, **141**, 15942–15950.

8 D. Micheroni, G. Lan and W. Lin, *J. Am. Chem. Soc.*, 2018, **140**, 15591–15595.
9 S. Pullen, H. Fei, A. Orthaber, S. M. Cohen and S. Ott, *J. Am. Chem. Soc.*, 2013, **135**, 16997–17003.
10 M. B. Chambers, X. Wang, N. Elgrishi, C. H. Hendon, A. Walsh, J. Bonnefoy, J. Canivet, E. A. Quadrelli, D. Farrusseng, C. Mellot-Draznieks and M. Fontecave, *ChemSusChem*, 2015, **8**, 603–608.
11 T. Kajiwara, M. Fujii, M. Tsujimoto, K. Kobayashi, M. Higuchi, K. Tanaka and S. Kitagawa, *Angew. Chem., Int. Ed.*, 2016, **55**, 2697–2700.
12 N. Kornienko, Y. Zhao, C. S. Kley, C. Zhu, D. Kim, S. Lin, C. J. Chang, O. M. Yaghi and P. Yang, *J. Am. Chem. Soc.*, 2015, **137**, 14129–14135.
13 I. Hod, M. D. Sampson, P. Deria, C. P. Kubiak, O. K. Farha and J. T. Hupp, *ACS Catal.*, 2015, **5**, 6302–6309.
14 H. Fei, M. D. Sampson, Y. Lee, C. P. Kubiak and S. M. Cohen, *Inorg. Chem.*, 2015, **54**, 6821–6828.
15 C. Wang, Z. Xie, K. E. deKrafft and W. Lin, *J. Am. Chem. Soc.*, 2011, **133**, 13445–13454.
16 C. Wang, J.-L. Wang and W. Lin, *J. Am. Chem. Soc.*, 2012, **134**, 19895–19908.
17 S. Lin, Y. Pineda-Galvan, W. A. Maza, C. C. Epley, J. Zhu, M. C. Kessinger, Y. Pushkar and A. J. Morris, *ChemSusChem*, 2017, **10**, 514–522.
18 S. Lin, A. K. Ravari, J. Zhu, P. M. Usov, M. Cai, S. R. Ahrenholtz, Y. Pushkar and A. J. Morris, *ChemSusChem*, 2018, **11**, 464–471.
19 A. Bhunia, B. A. Johnson, J. Czapla-Masztafiak, J. Sá and S. Ott, *Chem. Commun.*, 2018, **54**, 7770–7773.
20 B. A. Johnson, A. Bhunia and S. Ott, *Dalton Trans.*, 2017, **46**, 1382–1388.
21 A. W. Stubbs, L. Braglia, E. Borfecchia, R. J. Meyer, Y. Román-Leshkov, C. Lamberti and M. Dincă, *ACS Catal.*, 2018, **8**, 596–601.
22 E. D. Metzger, C. K. Brozek, R. J. Comito and M. Dincă, *ACS Cent. Sci.*, 2016, **2**, 148–153.
23 V. Pascanu, G. González Miera, A. K. Inge and B. Martín-Matute, *J. Am. Chem. Soc.*, 2019, **141**, 7223–7234.
24 L. Ma, C. Abney and W. Lin, *Chem. Soc. Rev.*, 2009, **38**, 1248–1256.
25 M. Yoon, R. Srirambalaji and K. Kim, *Chem. Rev.*, 2012, **112**, 1196–1231.
26 *Report of the Basic Energy Sciences Roundtable on Liquid Solar Fuels*, US Department of Energy, Rockville, Maryland, 2019, https://science.osti.gov/bes/Community-Resources/Reports.
27 D. Yang, M. A. Ortuño, V. Bernales, C. J. Cramer, L. Gagliardi and B. C. Gates, *J. Am. Chem. Soc.*, 2018, **140**, 3751–3759.
28 D. Yang, C. A. Gaggioli, D. Ray, M. Babucci, L. Gagliardi and B. C. Gates, *J. Am. Chem. Soc.*, 2020, **142**(17), 8044–8056.
29 E. S. Gutterød, S. Øien-Ødegaard, K. Bossers, A.-E. Nieuwelink, M. Manzoli, L. Braglia, A. Lazzarini, E. Borfecchia, S. Ahmadigoltapeh, B. Bouchevreau, B. T. Lønstad-Bleken, R. Henry, C. Lamberti, S. Bordiga, B. M. Weckhuysen, K. P. Lillerud and U. Olsbye, *Ind. Eng. Chem. Res.*, 2017, **56**, 13206–13218.
30 D. Yang and B. C. Gates, *ACS Catal.*, 2019, **9**, 1779–1798.
31 S. R. Ahrenholtz, C. C. Epley and A. J. Morris, *J. Am. Chem. Soc.*, 2014, **136**, 2464–2472.
32 S. Lin, P. M. Usov and A. J. Morris, *Chem. Commun.*, 2018, **54**, 6965–6974.
33 C. P. Andrieux and J. M. Savéant, *J. Electroanal. Chem. Interfacial Electrochem.*, 1980, **111**, 377–381.
34 E. Laviron, *J. Electroanal. Chem. Interfacial Electrochem.*, 1980, **112**, 1–9.
35 H. S. Fogler, *Elements of Chemical Reaction Engineering*, Pearson Education Inc., 5th edn, 2016.
36 J. Kärger, D. M. Ruthven and D. N. Theodorou, *Diffusion in Nanoporous Materials*, Wiley-VCH Verlag GmbH & Co. KGaA, 2012.
37 B. Zhang and L. Sun, *J. Am. Chem. Soc.*, 2019, **141**, 5565–5580.
38 L. Duan, F. Bozoglian, S. Mandal, B. Stewart, T. Privalov, A. Llobet and L. Sun, *Nat. Chem.*, 2012, **4**, 418–423.
39 X. Sala, S. Maji, R. Bofill, J. García-Antón, L. Escriche and A. Llobet, *Acc. Chem. Res.*, 2014, **47**, 504–516.
40 D. W. Shaffer, Y. Xie and J. J. Concepcion, *Chem. Soc. Rev.*, 2017, **46**, 6170–6193.
41 J. J. Concepcion, M.-K. Tsai, J. T. Muckerman and T. J. Meyer, *J. Am. Chem. Soc.*, 2010, **132**, 1545–1557.
42 P. N. Bartlett and K. F. E. Pratt, *J. Electroanal. Chem.*, 1995, **397**, 61–78.
43 R. Swaminathan, K. Lakshmi Narayanan, V. Mohan, K. Saranya and L. Rajendran, *Int. J. Electrochem. Sci.*, 2019, **2019**, 3777–3791.
44 M. E. G. Lyons, J. C. Greer, C. A. Fitzgerald, T. Bannon and P. N. Barlett, *Analyst*, 1996, **121**, 715–731.
45 E. W. Thiele, *Ind. Eng. Chem.*, 1939, **31**, 916–920.
46 R. M. Koros and E. J. Nowak, *Chem. Eng. Sci.*, 1967, **22**, 470.
47 R. J. Madon and M. Boudart, *Ind. Eng. Chem. Fundam.*, 1982, **21**, 438–447.
48 M. E. Davis and R. J. Davis, *Fundamentals of Chemical Reaction Engineering*, McGraw-Hill, New York, 1st edn, 2003.
49 Z. Chen, J. J. Concepcion, X. Hu, W. Yang, P. G. Hoertz and T. J. Meyer, *Proc. Natl. Acad. Sci. U. S. A.*, 2010, **107**, 7225–7229.
50 G. S. Mohammad-Pour, K. O. Hatfield, D. C. Fairchild, K. Hernandez-Burgos, J. Rodríguez-López and F. J. Uribe-Romo, *J. Am. Chem. Soc.*, 2019, **141**, 19978–19982.

